Quasi Steady-State Modeling and Characterization of Diffusion-Controlled Dissolution from Monodisperse Prolate and Oblate Spheroidal Particles

Yanxing Wang^{1,*}, Hui Wan², Tie Wei³, Dominick Nevares¹, and Fangjun Shu¹,

¹Department of Mechanical and Aerospace Engineering, New Mexico State University, Las Cruces, NM 88011, USA ²Department of Mechanical and Aerospace Engineering, University of Colorado, Colorado Springs, CO 80918, USA ³Department of Mechanical Engineering, New Mexico Institute of Mining and Technology, Socorro, NM 87801, USA

A quasi steady-state model of the dissolution of a single prolate or oblate spheroidal particle has been developed based on the exact solution of the steady-state diffusion equation for mass transfer in an unconfined media. With appropriate treatment of bulk concentration, the model can predict the detailed dissolution process of a single particle in a container of finite size. The dimensionless governing equations suggest that the dissolution process is determined by three dimensionless control parameters, initial solid particle concentration, particle aspect ratio, and the product of specific volume of solid particles and saturation concentration of the dissolved substance. Using this model, the dissolution process of felodipine particles are analyzed in a broad range of space of the three control parameters and some characteristics are identified. The effects of material properties indicated by the product of specific volume and saturation concentration are also analyzed. The model and the analysis are applicable to the system of monodisperse spheroidal particles of the same shape.

1. Introduction

Solid particle dissolution is ubiquitous in nature, and occurs in a wide spectrum of scientific and industrial applications, from traditional drug delivery [1] and metal ore heap leaching [2] to emerging renewable biomass energy [3] and dissolvable microrobots [4]. Among these applications, dissolution kinetics has been most intensively studied in the area of pharmaceuticals.

^{*}yxwang@nmsu.edu

The dissolution characteristics of drug particles are key to determining and manipulating drug release and the bioavailability of active pharmaceutical ingredients, and it is therefore vital to understand the physical and chemical processes involved.

The transport of dissolved molecules from particle surface to the surrounding fluid relies on both molecular diffusion and hydrodynamics around the particle. In some applications, such as drug dissolution in the gastrointestinal tract, the particle size is in the range from a few microns to hundreds of microns [5,6]. For such small particles, hydrodynamic effect is very weak and molecular diffusion plays a dominant role in mass transfer. So far, a large number of diffusiondominated dissolution models have been developed and broadly used in different areas [7]. However, most of the models are empirical or semi-empirical models that lack rigorous mathematical proof, and thus have a very narrow scope of application. A lot of effort was put into adjusting the parameters of the models according to the specific working conditions [8,9]. Among these models, the most widely used models are the Fick's-first-law-based Noyes-Whitney Model and its modification [7]. The basic idea is to establish a linear relationship between the particle dissolution rate and the concentration difference between particle surface and bulk fluid. The models usually involve a parameter called diffusion layer thickness, which is based on the recognition that a layer of high concentration fluid exists adjacent to the particle surface [7,10,11]. For spherical particles, the diffusion layer thickness is considered equal to the particle radius. These models have been shown to accurately predict the entire dissolution process of spherical particles. For non-spherical particles, the use of these models is greatly limited due to the inherent flaws in the models and the complexity of the diffusion layer thickness. It is believed that more than 70% of the solid particles in nature and practical applications are not regularly spherical, and the particle aspect ratio varies over a wide range from O(0.1) to O(10) [12-14]. The morphology has been found to play a key role in the dissolution process [12-14]. The assumption of spherical particles might be one of the dominant sources of error in quantifying the dissolution process. As a further extension of the current model development strategy, a simple and reliable model with a better prediction of the dissolution of spheroidal particles, including oblate and prolate ellipsoids, is highly required.

In a previous study, we critically examined the accuracy of several mathematical models built on the solutions of the diffusion equation to predict the details of diffusion-dominated dissolution of a single spherical particle [15]. The purpose was to identify a dissolution model that better balances accuracy with practicality of use. We found that a relatively simple "quasi steady-state" model (QSM) predicts both the increase in bulk concentration and the surface flux with high-level of accuracy beyond a short initial transient period. The advantages of QSM are that it is based on the exact solution to the steady-state diffusion equation and has a simple form.

In this paper, we build on our previous work and extend the QSM for spherical particles to that for prolate and oblate spheroidal particles. The model is based on the analytical solutions of the steady-state diffusion equation in spheroidal coordinate systems. According to the spatial distribution of molar concentration in the surrounding fluid, the detailed dissolution process, such as molar flux of dissolved substance and regression rate of particle surface will be acquired. The current study aims to develop a physics-based, easy and accurate dissolution model for spheroidal particles, and to substantially advance the understanding of the dissolution kinetics of non-spherical particles. This model establishes a solid foundation for the future development of more complex dissolution models considering hydrodynamics around the particles.

2. Mathematical model formulations

(a) General framework of quasi steady-state model

The quasi steady-state model (QSM) assumes that the time rate of change of the concentration of dissolved substance is negligible at every point and the spatial distribution of concentration satisfies the steady-state diffusion equation. The justification of this assumption is based on the relatively slow regression rate of particle surface. The characteristic time it takes for a dissolved substance to diffuse a distance L is L^2/D_m , where D_m is the diffusion coefficient. The characteristic time it takes for a particle surface to dissolve a distance L is $L^2/v_mC_sD_m$, where v_m is the specific volume of solid particles with units in volume/mol and C_s is the concentration at particle surface with units in mol/volume. For most solid chemicals, the ratio of diffusion to dissolution time scale is much smaller. For example, the ratio of time scales of felodipine, a drug which is used to treat high blood pressure, is 2.2×10^{-5} [15]. The basic idea of QSM is shown in Fig. 1. The solution of the steady-state diffusion equation ($\nabla^2 C = 0$) for the diffusion of dissolved substance around a particle in an infinitely large domain is,

$$C(\mathbf{r}) = f(\mathbf{r}) + C_{\infty} \tag{1}$$

where $C(\mathbf{r})$ is the concentration, $f(\mathbf{r})$ is a function of spatial coordinate \mathbf{r} and $f(\mathbf{r}) = 0$ at $|\mathbf{r}| = \infty$, and C_{∞} is the concentration at $|\mathbf{r}| = \infty$. At particle surface, the release flux $(N_S^{"})$ can be obtained from the spatial distribution of concentration (Eqn. (1)) as,

$$N_{S}^{"} = -D_{m} \frac{\partial c}{\partial n} \Big|_{\mathbf{r} = \mathbf{r}_{S}} \tag{2}$$

When the particle is put in a container with finite size, it is assumed that the concentration (C) described by Eqn. (1) is still applicable. The spatial integration of concentration in the container is the amount of substance released from the particle,

$$\int_{V_c} C(\mathbf{r}) dV = C_b V_c \tag{3}$$

where C_b is the average concentration in the bulk fluid, and V_c is the container volume. The amount of dissolved substance can also be obtained from the integration of surface flux over time (t),

$$\int_0^t \int_{A_n} N_S^{"} dA \, dt = C_b V_c \tag{4}$$

At every time step, the increase in bulk concentration (C_b) is evaluated from the integration of surface flux at previous time step and C_{∞} is calculated according to C_b . Then surface flux $(N_S^{"})$ and particle surface profile are updated according to the new C_{∞} . Time is advanced to the next step. In this model, the virtual concentration at infinity (C_{∞}) exists only as a link between $N_S^{"}$ and C_b . It's apparent that the QSM is applicable only when the particle size is much smaller than the container volume. The current research on dissolution mainly focuses on the dissolution of substances that do not dissolve easily, that is, the solubility is small. In these applications, the particle size is much smaller than the container volume.

The QSM for single particles also models the dissolution of monodisperse particles when assuming that the particles are uniformly distributed in the container. The QSM has found to be nearly as accurate as the exact solution for the diffusion-dominated dissolution of a spherical particle [15]. It also has a very concise form. These advantages make it the basis for the development of the complex models of non-spherical particle dissolution in this study.

(b) Steady-state diffusion equation for prolate and oblate spheroidal particles

The surface of an ellipsoidal particle is described by

$$\frac{x^2 + y^2}{a_p^2} + \frac{z^2}{b_p^2} = 1 \tag{5}$$

where x, y and z are Cartesian coordinates, a_p is the equatorial radius, and b_p is the polar radius. The aspect ratio is defined as,

$$\Lambda = a_p / b_p \tag{6}$$

When $\Lambda > 1$, the particle shape is oblate spheroidal, when $\Lambda < 1$, the shape is prolate spheroidal, and when $\Lambda = 1$, the shape is spherical.

Under the quasi steady-state assumption, the concentration around a particle in a quiescent liquid is described by the steady-state diffusion equation,

$$\nabla^2 C(x, y, z) = 0 \tag{7}$$

where C(x, y, z) (mol/volume) is the molar concentration of dissolved substance. At the particle surface, the concentration (C_S) is the saturated concentration (C_{sat}) which is constant.

$$C_S = C_{sat} (8)$$

The molar flux of dissolved substance from the particle surface to the surrounding liquid, N_S (mol/area-time), is defined as

$$N_{S}^{"} = -D_{m}\vec{n} \cdot \nabla C|_{S} \tag{9}$$

where D_m is the diffusion coefficient for the dissolve substance in the fluid, and \vec{n} is a unit normal vector pointing outwards to the ambient fluid. The particle surface regresses with time as the particle loses mass from its surface,

$$\frac{dR_n}{dt} = -N_S^{"} v_m \tag{10}$$

where R_n is the surface coordinate in the direction normal to particle surface, and v_m (volume/mol) is the specific volume of the solid particle. For a given particle, the dissolution process also depends on the container volume, which confines the dissolved substance within the container. From the initial particle volume (V_{p0}) and container volume (V_c) , the initial solid particle concentration, C_{p0} (mol/volume), is calculated as

$$C_{p0} \equiv \frac{V_{p0}}{v_m V_c} \tag{11}$$

In the calculation, either V_c or C_{p0} can be used to specify the container volume. Equations (5-11) constitute the formulations describing the dissolution process of a single particle.

Each spheroidal particle has a corresponding spherical particle whose volume is the same as the initial volume of the spheroidal particle. The radius of the spherical particle is given as,

$$R_0 = \left(a_{p0}^2 b_{p0}\right)^{1/3} \tag{12}$$

where a_{p0} and c_{p0} are the equatorial and polar radii of the spheroids at t = 0. Using R_0 and C_{sat} as the characteristic quantities, Eqns. (5-9) can be nondimensionalized as,

$$\frac{\tilde{x}^2 + \tilde{y}^2}{\tilde{a}_p^2} + \frac{\tilde{z}^2}{\tilde{b}_p^2} = 1 \tag{13}$$

$$\Lambda = \tilde{a}_p / \tilde{b}_p \tag{14}$$

$$\widetilde{\nabla}^2 \widetilde{C}(\widetilde{x}, \widetilde{y}, \widetilde{z}) = 0 \tag{15}$$

$$\tilde{C}_{S} = 1 \tag{16}$$

$$\widetilde{N_S''} = -\frac{\partial \widetilde{C}}{\partial \tilde{n}}\Big|_{S} \tag{17}$$

where $\tilde{x} = x/R_0$, $\tilde{y} = y/R_0$, $\tilde{z} = z/R_0$, $\tilde{a}_p = a_p/R_0$, $\tilde{b}_p = b_p/R_0$, $\tilde{\nabla} = R_0 \nabla$, $\tilde{C} = C/C_{sat}$, and $\widetilde{N_S} = N_S''/(D_m C_{sat}/R_0)$. The time for a spherical particle to fully dissolve in an infinite fluid medium is [15]

$$\tau_{diss} = \frac{R_0^2}{2v_m C_{sat} D_m} \tag{18}$$

Using τ_{diss} to nondimensionalize the time ($\tilde{t} = t/\tau_{diss}$), Eqn. (10) is nondimensionalized as,

$$\frac{d\tilde{R}_n}{d\tilde{t}} = -\frac{1}{2}\widetilde{N_S''} \tag{19}$$

The initial solid particle concentration (Eqn. (11)) is normalized as

$$\tilde{C}_{p0} = (\tilde{V}_{p0}/\tilde{V}_c)/(C_{sat}v_m)$$
(20)

where
$$\tilde{C}_{p0} = C_{p0}/C_{sat}$$
, $\tilde{V}_{p0} = V_{p0}/R_0^3$, and $\tilde{V}_c = V_c/R_0^3$.

Equations (13-20) constitute the complete system of equations describing the dissolution process of a single prolate or oblate spheroidal particle in the dimensionless space. Any specific dissolution process can be determined by three controlling parameters, Λ , \tilde{C}_{p0} , and $(C_{sat}v_m)$. Compared with the dimensional space, the number of controlling parameters is significantly reduced in the dimensionless space. In order to connect with the real physical mechanism, the following derivation and analysis are carried out in the physical space.

At present, we do not have a rigorous mathematical proof that the shape of the prolate and oblate spheroidal particles does not change during dissolution. The derivation below (Eqns. (32) and (57)) shows that the ratio of the dissolution rate at the equator to that at the pole is equal to the ratio of the equatorial radius to the polar radius. Thus, the shape invariance is a reasonable assumption.

(c) Dissolution of prolate spheroidal particles

For the prolate spheroidal particle, the prolate spheroidal coordinates (ξ, η, ϕ) is utilized instead of the Cartesian coordinates (x, y, z) (Fig. 2). The conversion between the two coordinate systems are,

$$x = \Omega \sinh \xi \sin \eta \cos \phi \tag{21}$$

$$y = \Omega \sinh \xi \sin \eta \sin \phi \tag{22}$$

$$z = \Omega \cosh \xi \cos \eta \tag{23}$$

where ξ is a nonnegative real number and the angles $\eta \in [0, \pi]$, $\phi \in [0, 2\pi]$. Curves of constant ξ and η on the (y, z) plane are half-ellipse and half-hyperbolae with focus at $(y, z) = (0, \pm \Omega)$, and

$$\Omega = \sqrt{b_p^2 - a_p^2} \tag{24}$$

The prolate spheroidal particle surface is described by constant ξ (= ξ_S). ξ_S can be acquired from the surface point at the pole $(x, y, z) = (0,0,b_p)$ according to Eqn. (23),

$$\xi_S = \operatorname{arccosh}\left(\frac{b_p}{a}\right) = \operatorname{arccosh}\left(b_p/\sqrt{b_p^2 - a_p^2}\right)$$
 (25)

In the prolate spheroidal system, the Laplace equation (Eqn. (7)) becomes,

$$\nabla^2 C(\xi, \eta, \phi)$$

$$= \frac{1}{\Omega^2(\sinh^2\xi + \sin^2\eta)} \left[\frac{\partial^2 C}{\partial \xi^2} + \coth\xi \frac{\partial C}{\partial \xi} + \frac{\partial^2 C}{\partial \eta^2} + \cot\eta \frac{\partial C}{\partial \eta} \right] + \frac{1}{\Omega^2(\sinh^2\xi + \sin^2\eta)} \frac{\partial^2 C}{\partial \phi^2}$$

$$= 0 \tag{26}$$

It is reasonable to assume that the distribution of concentration (C) is axisymmetric about z axis, then C becomes independent of ϕ and $\partial^2 C/\partial \phi^2 = 0$. Using separation of variables, the concentration is written as $C(\xi, \eta, \phi) = E(\xi)N(\eta)$. At particle surface, $\xi = \xi_S$ and $C = C_{sat}$, so $N(\eta)$ becomes a constant. By solving the differential equation, the concentration is acquired as

$$C(\xi, \eta, \phi) = A \ln\left(\tanh\frac{\xi}{2}\right) + B \tag{27}$$

where A and B are the constants that will be determined from the boundary conditions. At the particle surface, $C(\xi = \xi_s) = A \ln \left(\tanh \frac{\xi_s}{2} \right) + B = C_{sat}$. In the far field, $C(\xi \to \infty) = A \ln \left(\tanh \frac{\xi}{2} \right) \Big|_{\xi \to \infty} + B = C_{\infty}$. A and B then can be acquired as,

$$A = \frac{c_{sat} - c_{\infty}}{\ln\left(\tanh\frac{\xi_s}{2}\right)} \tag{28}$$

$$B = C_{\infty} \tag{29}$$

The molar flux at the particle surface can be calculated from the gradience of the concentration at the surface, i.e.,

$$N_S'' = -D_m \frac{\partial \mathcal{C}}{\partial n} \Big|_{S} = -D_m \frac{1}{h_{\xi}} \frac{\partial \mathcal{C}}{\partial \xi} \Big|_{S} = -D_m \frac{1}{h_{\xi}} \frac{A}{\sinh \xi_S}$$
(30)

where h_{ξ} is the scale factor for coordinate ξ , and

$$h_{\xi} = \Omega \sqrt{\sinh^2 \xi + \sin^2 \eta} \tag{31}$$

At $\eta=0$ and π (poles), $h_{\xi}=a_{p}$, and at $\eta=\pi/2$ (equator), $h_{\xi}=b_{p}$. Therefore,

$$\frac{N_{S,\eta=\pi/2}^{"}}{N_{S,n=0}^{"}} = \frac{a_p}{b_p} \tag{32}$$

This suggests that the ratio of particle regression rate on the equator to that at the poles is equal to the ratio of equatorial radius to polar radius. This partly supports the conclusion that the particle shape maintains spheroidal and the aspect ratio remains constant.

The release rate through particle surface N_s' (mol/time) equals the integration of N_s'' at the particle surface,

$$N_S' = \int_{A_n} N_S'' dA_p = \int_0^{\pi} \int_0^{2\pi} N_S'' h_{\eta} h_{\phi} d\eta d\phi = -4\pi A D_m \Omega$$
 (33)

where A_p is the area of particle surface, h_η and h_ϕ are the scale factors for coordinates η and ϕ , and

$$h_n = \Omega \sqrt{\sinh^2 \xi + \sin^2 \eta} \tag{34}$$

$$h_{\phi} = \Omega \sinh \xi \sin \eta \tag{35}$$

We assume that the particle is placed at the center of a spheroidal container and ξ coordinate is constant at the container surface. The focuses of the spheroidal container are the same as that of the spheroidal particle, so we have

$$\Omega = \sqrt{b_c^2 - a_c^2} \tag{36}$$

where a_c and b_c are the primary and minor axes of the container, and are unknown. The container volume is given as,

$$V_c = \frac{4}{3}\pi a_c^2 b_c \tag{37}$$

 a_c and b_c can be obtained by solving Eqns. (36) and (37),

$$b_c = \sqrt[3]{-\frac{q}{2} + \sqrt{\frac{q^2}{4} + \frac{p^3}{27}}} + \sqrt[3]{-\frac{q}{2} - \sqrt{\frac{q^2}{4} + \frac{p^3}{27}}}$$
(38)

$$a_c = \sqrt{b_c^2 - \Omega^2} \tag{39}$$

where $p=-\Omega^2$ and $q=-\frac{3V_c}{4\pi}$. Then the ξ coordinate at container surface is,

$$\xi_c = \operatorname{arccosh}\left(\frac{b_c}{\Omega}\right) \tag{40}$$

The amount of dissolved substance in the liquid (N) can be obtained by integrating the concentration in the container,

$$N = \int_{c} C(\xi, \eta, \phi) dV = \iiint_{c} C(\xi, \eta, \phi) h_{\xi} h_{\eta} h_{\phi} d\xi d\eta d\phi = J_{1}A + J_{2}A + J_{3}B + J_{4}B$$
 (41)

where

$$J_1 = 4\pi\Omega^3 \left[\frac{1}{3} \ln \left(\frac{\cosh \xi - 1}{\sinh \xi} \right) \cosh^3 \xi \right]_{\xi_S}^{\xi_C} + \frac{2}{3} \ln \left(\sinh \xi \right) \Big|_{\xi_S}^{\xi_C} - \frac{1}{6} \sinh^2 \xi \Big|_{\xi_S}^{\xi_C} - \ln \left(\frac{\cosh \xi - 1}{\sinh \xi} \right) \cosh \xi \Big|_{\xi_S}^{\xi_C} \right]$$

$$J_2 = \frac{8}{3}\pi\Omega^3 \left[\ln \left(\frac{\cosh \xi - 1}{\sinh \xi} \right) \cosh \xi \, |_{\xi_S}^{\xi_c} - \ln (\sinh \xi) \, |_{\xi_S}^{\xi_c} \right]$$

$$J_3 = 4\pi\Omega^3 \left[\frac{1}{3} \cosh^3 \xi \, |_{\xi_S}^{\xi_C} - \cosh \xi \, |_{\xi_S}^{\xi_C} \right]$$

$$J_4 = \frac{8}{3}\pi\Omega^3 \cosh\xi \mid_{\xi_S}^{\xi_C} \tag{42}$$

Let C_b be the bulk concentration in the liquid. The amount of substance dissolved in the liquid can also be calculated as

$$N = C_b V_c = \frac{4}{3} \pi C_b \left(a_c^2 b_c - a_p^2 b_p \right)$$
 (43)

Equating Eqns. (41) and (43) gives,

$$J_1 A + J_2 A + J_3 B + J_4 B = \frac{4}{3} \pi C_b \left(a_c^2 b_c - a_p^2 b_p \right)$$
 (44)

Substituting Eqns. (28) and (29) into (44) gives,

$$C_{\infty} = \left[\frac{(J_1 + J_2)}{\ln(\tanh\frac{\xi_S}{2})} C_{sat} - \frac{4}{3}\pi C_b \left(a_c^2 b_c - a_p^2 b_p \right) \right] / \left[\frac{(J_1 + J_2)}{\ln(\tanh\frac{\xi_S}{2})} - (J_3 + J_4) \right]$$
(45)

(d) Dissolution of oblate spheroidal particles

For the oblate spheroidal particle, the oblate spheroidal coordinates system (ξ, η, ϕ) is shown in Fig. 3. The conversion between the Cartesian and oblate spheroidal systems are,

$$x = \Omega \cosh \xi \cos \eta \cos \phi \tag{46}$$

$$y = \Omega \cosh \xi \cos \eta \sin \phi \tag{47}$$

$$z = \Omega \sinh \xi \sin \eta \tag{48}$$

where ξ is a nonnegative real number and the angles $\eta \in [-\pi/2, \pi/2]$, $\phi \in [0,2\pi]$. Curves of constant ξ and η on the (y,z) plane are half-ellipse and half-hyperbolae with focus at $(y,z) = (\pm \Omega, 0)$, and

$$\Omega = \sqrt{a_p^2 - b_p^2} \tag{49}$$

The oblate spheroidal particle surface is described by constant ξ (= ξ_S). ξ_S can be acquired from the surface point on the minor axis $(x, y, z) = (0,0, b_p)$ according to Eqn. (48),

$$\xi_S = \operatorname{arcsinh}\left(\frac{b_p}{a}\right) = \operatorname{arcsinh}\left(b_p/\sqrt{a_p^2 - b_p^2}\right)$$
 (50)

In the oblate spheroidal system, the Laplace equation (Eqn. (7)) becomes,

$$\nabla^{2}C(\xi,\eta,\phi)$$

$$= \frac{1}{\Omega^{2}(\sinh^{2}\xi + \sin^{2}\eta)} \left[\frac{1}{\cosh\xi} \frac{\partial}{\partial\xi} \left(\cosh\xi \frac{\partial C}{\partial\xi} \right) + \frac{1}{\cos\eta} \frac{\partial}{\partial\eta} \left(\cos\eta \frac{\partial C}{\partial\eta} \right) \right] + \frac{1}{\Omega^{2}(\cosh^{2}\xi + \cos^{2}\eta)} \frac{\partial^{2}C}{\partial\phi^{2}}$$

$$= 0$$
(51)

With the axisymmetric assumption, C is independent of ϕ and $\partial^2 C/\partial \phi^2 = 0$. Using separation of variables, the concentration is written as $C(\xi, \eta, \phi) = E(\xi)N(\eta)$. At particle surface $\xi = \xi_S$ and $C = C_{sat}$, so $N(\eta)$ becomes a constant. By solving the differential equation, the concentration is acquired as

$$C(\xi, \eta, \phi) = A \arctan(\sinh \xi) + B \tag{52}$$

where A and B are the constants that will be determined by the boundary conditions. At particle surface, $C(\xi = \xi_S) = A \arctan(\sinh \xi_S) + B = C_{sat}$. In the far field, $C(\xi \to \infty) = A \arctan(\sinh \xi)|_{\xi \to \infty} + B = C_{\infty}$. A and B can be acquired as,

$$A = \frac{c_{sat} - c_{\infty}}{\arctan(\sinh \xi_S) - \pi/2} = \frac{c_{sat} - c_{\infty}}{\arctan(b_p/\Omega) - \pi/2}$$
(53)

$$B = C_{\infty} - \frac{\pi}{2}A = C_{\infty} - \frac{\pi}{2} \frac{C_{sat} - C_{\infty}}{\arctan(b_n/\Omega) - \pi/2}$$

$$\tag{54}$$

The scalar flux on the particle surface is given as

$$N_S'' = -D_m \frac{\partial C}{\partial n}\Big|_S = -D_m \frac{1}{h_E} \frac{A}{\cosh \xi_S}$$
 (55)

where h_{ξ} is the scale factor for coordinate ξ , and

$$h_{\xi} = \Omega \sqrt{\sinh^2 \xi + \sin^2 \eta} \tag{56}$$

At $\eta = \pm \pi/2$ (poles), $h_{\xi} = a_p$, and at $\eta = 0$ (equator), $h_{\xi} = b_p$. Therefore,

$$\frac{N_{S,\eta=\pi/2}^{"}}{N_{S,\eta=0}^{"}} = \frac{a_p}{b_p} \tag{57}$$

For oblate particles, it is also true that the ratio of particle regression rate on the equator to that at the poles is equal to the ratio of equatorial radius to polar radius, thus the particle aspect ratio keeps constant during dissolution.

The release rate through particle surface N'_{S} (mol/time) equals the integration of N''_{S} at the particle surface,

$$N_S' = \int_{A_p} N_S'' dA_p = \int_{-\pi/2}^{\pi/2} \int_0^{2\pi} N_S'' h_\eta h_\phi d\eta d\phi = -4\pi A D_m \Omega$$
 (58)

where h_{η} and h_{ϕ} are the scale factors for coordinates η and ϕ , and

$$h_{\eta} = \Omega \sqrt{\sinh^2 \xi + \sin^2 \eta} \tag{59}$$

$$h_{\phi} = \Omega \cosh \xi \cos \eta \tag{60}$$

It is assumed that the particle is placed at the center of a spheroidal container and ξ coordinate is constant at the container surface. The focuses of the spheroidal container are the same as that of the spheroidal particle, so we have

$$\Omega = \sqrt{a_c^2 - b_c^2} \tag{61}$$

where a_c and c_c are the primary and minor axes of the container, and are unknown. The container volume is given as,

$$V_c = \frac{4}{3}\pi a_c^2 b_c \tag{62}$$

 a_c and b_c can be obtained by solving Eqns. (61) and (62),

$$b_c = \sqrt[3]{-\frac{q}{2} + \sqrt{\frac{q^2}{4} + \frac{p^3}{27}}} + \sqrt[3]{-\frac{q}{2} - \sqrt{\frac{q^2}{4} + \frac{p^3}{27}}}$$
(63)

$$a_c = \sqrt{\Omega^2 + b_c^2} \tag{64}$$

where $p = \Omega^2$ and $q = -\frac{3V_c}{4\pi}$. Then the ξ coordinate at container surface is given as,

$$\xi_c = \operatorname{arcsinh}\left(\frac{b_c}{a}\right) \tag{65}$$

The amount of dissolved substance in the liquid can be obtained by integrating the concentration in the container,

$$N = \int_{C} C(\xi, \eta, \phi) dV = \iiint_{C} C(\xi, \eta, \phi) h_{\xi} h_{\eta} h_{\phi} d\xi d\eta d\phi = J_{1}A + J_{2}A + J_{3}B + J_{4}B$$
 (66)

where

$$J_{1} = \frac{4}{3}\pi\Omega^{3} \left\{ \operatorname{arctan}(\epsilon) \epsilon^{3} \Big|_{\sinh \xi_{S}}^{\sinh \xi_{C}} - \frac{1}{2} [(1 + \epsilon^{2}) - \ln(1 + \epsilon^{2})] \Big|_{\sinh \xi_{S}}^{\sinh \xi_{C}} \right\}$$

$$J_{2} = \frac{4}{3}\pi\Omega^{3} \left\{ \operatorname{arctan}(\epsilon) \epsilon \Big|_{\sinh \xi_{S}}^{\sinh \xi_{C}} - \frac{1}{2} \ln(1 + \epsilon^{2}) \Big|_{\sinh \xi_{S}}^{\sinh \xi_{C}} \right\}$$

$$J_{3} = \frac{4}{3}\pi\Omega^{3} \epsilon^{3} \Big|_{\sinh \xi_{S}}^{\sinh \xi_{C}}$$

$$J_{4} = \frac{4}{3}\pi\Omega^{3} \epsilon \Big|_{\sinh \xi_{C}}^{\sinh \xi_{C}}$$
(67)

The amount of substance dissolved in the liquid can also be calculated as

$$N = C_b V_c = \frac{4}{3} \pi C_b \left(a_c^2 b_c - a_p^2 b_p \right)$$
 (68)

Equating Eqns. (66) and (68) gives,

$$J_1 A + J_2 A + J_3 B + J_4 B = \frac{4}{3} \pi C_b \left(a_c^2 b_c - a_p^2 b_p \right)$$
 (69)

Substituting Eqns. (53) and (54) into (69) gives,

$$C_{\infty} = \left\{ \left[\frac{(J_1 + J_2)}{D} - \frac{\pi}{2} \frac{(J_3 + J_4)}{D} \right] C_{sat} - \frac{4}{3} \pi C_b \left(a_c^2 b_c - a_p^2 b_p \right) \right\} / \left[\frac{(J_1 + J_2)}{D} - \frac{\pi}{2} \frac{(J_3 + J_4)}{D} - (J_3 + J_4) \right]$$
 (70) where $D \equiv \arctan(b_p/\Omega) - \pi/2$.

Analysis of dissolution process

(a) Research design

To test the model and explore the dissolution kinetics, we use drug-specific parameters of a commonly used drug for hypertension, felodipine. The molar volume of felodipine is $v_m = 265$ cm³/mol. The crystalline water solubility in density-matched water containing 38.6% w/w CsCl at 37 °C was measured to be $C_{sol} = 0.89 \,\mu\text{M}$. It is also the saturation concentration (C_{sat}) Using the stokes-Einstein equation, the reported value for the felodipine diffusion coefficient at 25 °C in pure water was calculated to be $D_m = 6.7 \times 10^{-6} \, \text{cm}^2/\text{s}$.

In the following section, we will use the model to analyze the dissolution characteristics of a single felodipine particle with spheroidal shape in a finite size container. It has been shown above that in the nondimensional space, the dissolution process is determined by three parameters, particle aspect ratio $\Lambda = a_p/b_p$, initial particle concentration $\tilde{C}_{p0} = C_{p0}/C_{sat}$, and the product of saturation concentration and specific volume of solid particle $(C_{sat}v_m)$. The effect of these three parameters on the dissolution characteristics will be the focus of the analysis.

(b) Model validation

To validate the model, we compare the prediction of QSM for single or monodisperse particles with experimental measurements of dissolution from polydisperse collections of felodipine drug particles in a Couette flow viscometer. In the experiment, the particle shapes are random and irregular, and the size distribution is represented as a Gaussian function of the logarithm of the particle radii (R_p). The single particle radius (3.34 μ m) is equal to the volume-averaged radius of the polydisperse collection. The details of the experiments are described by Lindfors et al. [16]. A simple laminar shear flow with closely linear velocity profile was created by rotating the inner cylinder of the Couette viscometer at 5 rpm, producing a low Reynolds number laminar flow that,

together with the small size of particles, produced highly diffusion-dominated dissolution from particles with random geometries. In Fig. 4, we compare the prediction of the time variation of bulk concentration (C_b) of QSM with the experimental measurements. Two initial particle concentrations are considered, $C_{p0} = 0.5$ and 1.5 μ M. In QSM, five aspect ratios are considered, $\Lambda = 1$, 1/5, 1/10, 5, and 10, corresponding to spherical, prolate, and oblate spheroidal particles. Overall, the predictions of the QSM are in good agreement with the experimental measurements. For the QSM prediction, C_b of spherical particle ($\Lambda = 1$) is smaller than that of prolate ($\Lambda < 1$) and oblate ($\Lambda > 1$) spheroidal particles at every time point. The particles in the experiments consist of a variety of shapes and a wide range of sizes, which resulted in a faster increase in bulk concentration than that of monodisperse spherical particles. That is why the QSM prediction for spheroidal particles are lower than that of experimental measurements. Yet the QSM prediction for spheroidal particles corrects the deviation to some extent. The conclusion is that the current single particle model is well validated with the experimental measurements, but more complex models considering various particle shapes and sizes are needed to deal with the particles in the real world.

(c) Prediction of bulk properties

The spatial distribution of molar concentration of the dissolved substance given by Eqns. (27) and (52) are functions of spheroidal coordinates (ξ, η, ϕ) . The coefficients (A and B) are functions of concentration at infinity (C_{∞}) , which increases with time (t). When normalizing the concentration as $\hat{C} \equiv (C - C_{\infty})/(C_s - C_{\infty})$, \hat{C} becomes independent of t. Figure 5 shows the distribution of \hat{C} around a prolate and an oblate spheroidal particle with $\Lambda = 0.5$ and 2, respectively. \hat{C} decreases from 1 at particle surfaces to 0 at infinity. Because of the larger curvature, \hat{C} changes more sharply near the poles of the prolate particle and near the equator of the oblate particle.

On particle surfaces, the molar flux $(N_S^")$ of dissolved substance changes with the spheroidal coordinate η . It also depends on the particle aspect ratio (Λ) . Figure 6 shows the variation of $N_S^"$ with η for different Λ . $N_S^"$ is normalized as $\widehat{N}_S^" \equiv N_S^"/(D_m(C_S-C_\infty)/R)$, where R is the radius of the spherical particle with the same volume as the spheroidal particle. For a spherical particle, $\widehat{N}_S^"$ is constant which is equal to 1. In Fig. 6(a), Λ increases from 0.9 to 1.1 with an increment of 0.02. For prolate spheroidal particles, $\widehat{N}_S^"$ is larger than 1 near the poles $(\eta = 0 \text{ and } \pi)$ and smaller than

1 near the equator $(\eta = \pi/2)$, With the increase in Λ toward 1, $\widehat{N}_S^{"}$ decreases toward 1 near the poles and increases toward 1 near the equator. For oblate spheroidal particles, $\widehat{N}_S^{"}$ is larger than 1 near the equator $(\eta = 0)$, and smaller than 1 near the poles $(\eta = \pm \pi/2)$. When Λ increases from 1, $\widehat{N}_S^{"}$ increases from 1 near the equator, and decreases from 1 near the poles. For both prolate and oblate particles, $\widehat{N}_S^{"}$ approaches the value of a spherical particle as Λ approaches 1. This trend also provides validation for the QSM proposed in this paper. This figure depicts the surface flux $(\widehat{N}_S^{"})$ as a function of spheroidal coordinate (η) and particle aspect ratio (Λ) . Fig. 6(b) shows the variation of $\widehat{N}_S^{"}$ in a wider range of Λ . For prolate particles, $\widehat{N}_S^{"}$ increases faster near the poles with the decrease in Λ and its variation with η becomes sharper. For oblate particles, the similar increase occurs near the equator.

When the initial concentration of solid particles is less than the saturation concentration ($C_{p,0}$ < C_{sat}), the solid particles will dissolve completely after a period of time. When $C_{p,0}$ is greater than C_{sat} , the dissolution will stop after the bulk concentration reaches the saturation concentration $(C_b = C_{sat})$, and the solid particles will remain in the solution with a smaller size. When $C_{p,0}$ is equal to C_{sat} , the particles will fully dissolve and the solution will be saturated ($C_b = C_{sat}$) in the end. Figure 7 shows the variation of C_b with time t. C_b is normalized with the concentration at particle surface (C_s) which is equal to the saturation concentration (C_{sat}) . t is normalized with the dissolution time τ_{diss} which is defined by Eqn. (18). Five values of $C_{p,0}/C_s$ are considered, which are $C_{p,0}/C_s = 0.01, 0.1, 1, 10$, and 100. The particle shapes include spherical, prolate spheroidal, and oblate spheroidal. The aspect ratios are $\Lambda = 1, 1/5, 5, 1/10$, and 10. As shown in the figure, it takes much longer for the particles to fully dissolve in the cases with $C_{p,0}/C_s=1$ than those with $C_{p,0}/C_S \neq 1$, because the surface flux $(N_S^{"})$ decreases as C_b approaches C_{sat} , and the decreased $N_S^{"}$ in turn reduces the increase in C_b . The cases with $C_{p,0}/C_s > 1$ also have the same situation, yet the relatively larger particle surface area shortens the period of C_b increase. For each $C_{p,0}/C_s$, C_b/C_s of spherical particle ($\Lambda = 1$) increases slower than that of prolate ($\Lambda < 1$) and oblate ($\Lambda > 1$) 1) spheroidal particles, because the surface release rates (N'_s) of spheroidal particles, which are described by Eqns. (33) and (58) are larger than that of spherical particles. For prolate spheroidal particles, C_b/C_s increases faster for smaller Λ . Yet for oblate spheroidal particles, C_b/C_s increases faster for larger Λ . This is consistent with the effect of aspect ratio on surface flux shown in Fig.

6. It is interesting that the curves of $\Lambda = 1/5$ are close to those of $\Lambda = 5$, and the curves of $\Lambda =$ 1/10 are close to those of $\Lambda = 10$. Yet the difference between the curves of $\Lambda = 1/10$ and 10 is larger than that between the curves of $\Lambda = 1/5$ and 5. There is no strict mathematical proof to suggest a direct relationship between the dissolution of prolate spheroidal particles with $\Lambda = 1/n$ and that of oblate particles with $\Lambda = n$. In addition, for each $C_{p,0}/C_s$ and n, C_b/C_s increases faster for prolate spheroid $(\Lambda = 1/n)$ than for oblate spheroid $(\Lambda = n)$, although the surface area of the prolate spheroid is smaller than that of the corresponding oblate spheroid. This is because that the surface flux $(\widehat{N}_{S}^{"})$ (Eqns. (30) and (55)) depends on the curvature of spheroidal surface through a complex relationship. On average, the prolate spheroid has greater surface curvature. This can be seen in the variation of surface flux shown in Fig. 6. In the initial period, the increase in C_b/C_s is less sensitive to the value of C_b/C_s , and C_b/C_s increases roughly linearly with time (t) in the linear-linear scales (Fig. 7(a)). With the increase in C_b/C_s , the nonlinear effect becomes more and more apparent and the curves are not straight any more. In the log-log scales (Fig. 7(b)), the curves are expanded in the regions of small t/τ_{diss} and small C_b/C_s , and all the curves are parallel to each other over the majority range of the logarithm of time. This is because that in the initial period, $C_b \approx 0$, and the curve slope described by $k = d(\log(C_b/C_s))/d(\log(t/\tau_{diss}))$ is equal to 1. The nonlinear effects of $C_{p,0}/C_s$ and Λ only becomes obvious when C_b/C_s is close to 1. This characteristic greatly facilitates the development of the simpler and more applicable empirical models.

According to Eqns. (32) and (57), the aspect ratio (Λ) of the spheroidal particles does not change during dissolution. Here we use the isovolumetric radius, $R_p \equiv \left(a_p^2 b_p\right)^{1/3}$, which is the radius of a spherical particle with the same volume as that of the spheroidal particle, to represent the time-varying particle size. This facilitates the comparison of particle size among the particles of different aspect ratios. Figure 8 shows the reduction of R_p with time for different $C_{p,0}/C_s$ and Λ . R_p is normalized with the initial radius of the spherical particle R_0 . As shown in the figure, R_p/R_0 decreases more sharply for smaller $C_{p,0}/C_s$. When $C_{p,0}/C_s < 1$, the curve slope approaches infinity as R_p/R_0 decreases towards 0. When $C_{p,0}/C_s > 1$, the curves have a long horizontal tail before the solution is saturated, because of the reduced surface flux (N_s^n) as C_b/C_s approaches 1. When $C_{p,0}/C_s = 1$, the dissolution time is infinity. For each $C_{p,0}/C_s$, R_p/R_0

decreases faster for smaller aspect ratio (Λ) for prolate spheroidal particles ($\Lambda < 1$), yet R_p/R_0 decreases faster for larger Λ for oblate particles ($\Lambda > 1$). This is consistent with the variation of bulk concentration C_b/C_s shown in Fig. 7.

(d) Prediction of Dissolution Rate and Sherwood Number

The surface flux of dissolved substance $(N_S^{"})$ for prolate and oblate spheroidal particles are given by Eqns. (30) and (55). The coefficient A is proportional to the difference of concentration at particle surface and infinity, $C_S - C_\infty$. Yet C_∞ changes with time during dissolution. In practical applications, bulk concentration C_b is more tangible than C_∞ . Therefore, it is more convenient to use the nondimensional flux, the so-called Sherwood number (Sh) to characterize the surface flux. For spherical particles, Sh has the form of

$$Sh \equiv \frac{N_S^{"}}{D_m(C_S - C_h)/R} \tag{71}$$

where R is particle radius which changes with time. For prolate and oblate particles, $N_S^{"}$ is not uniform at particle surface. Compared with the spherical particle having the same volume, the prolate and oblate spheroidal particles have larger surface areas, which increases the overall release rate. In order to evaluate the overall enhancement of dissolution rate, it's more convenient to define the Sherwood number for prolate and oblate spheroidal particles as,

$$Sh \equiv \frac{\int_{A_p} N_S^{"} dA_p / 4\pi R_p^2}{D_m (C_S - C_b) / R_p} = \frac{\int_{A_p} N_S^{"} dA_p}{4\pi R_p D_m (C_S - C_b)}$$
(72)

where R_p is the isovolumetric radius of the prolate and oblate spheroidal particles, and $4\pi R_p^2$ is the surface area of the spherical particle.

During dissolution, Sh changes with time (t). For different initial concentrations of solid particles $(C_{p,0}/C_s)$, the time it takes for the particles to fully dissolve or saturate the solution is different. Since bulk concentration (C_b) also changes with time, the variation of Sh with C_b will provide more insights. Figure 9 shows the plot of Sh versus C_b/C_s for three typical initial particle concentrations, $C_{p,0}/C_s = 1$, 0.1 and 10. Five aspect ratios are involved, $\Lambda = 1$, 1/5, 5, 1/10 and 10. For all $C_{p,0}$ and Λ , Sh remains roughly constant during the dissolution process, although slight

decrease can be observed for $C_{p,0}/C_s=0.1$. As shown in the figure, Λ plays a dominant role in determining Sh than $C_{p,0}/C_s$. For spherical particles ($\Lambda=1$), Sh ≈ 1 . This has been thoroughly analyzed in Wang et al. [15]. Both the decrease and increase in Λ from 1 can cause the increase in Sh. For prolate spheroidal particles with $\Lambda=1/5$ and oblate particles with $\Lambda=5$, the values of Sh are close to each other, which are between 1.2 and 1.3. For $\Lambda=1/10$ and $\Lambda=10$, the difference between two aspect ratios becomes apparent. The values of Sh are around 1.6 for $\Lambda=1/10$ and 1.5 for $\Lambda=10$, respectively, which are larger than those of $\Lambda=1/5$ and 5. Sh is also influenced by $C_{p,0}/C_s$. For each aspect ratio, $Sh_{C_{p,0}/C_s=10}>Sh_{C_{p,0}/C_s=1}>Sh_{C_{p,0}/C_s=0.1}$, that is, larger initial particle concentration has larger Sh.

As shown Fig. 9, Sh remains roughly constant during dissolution within wide ranges of $C_{p,0}/C_s$ and Λ . This characteristic suggests that Sh_0 , the Sh at t=0 can be used to compare the dissolution rates among the cases with different $C_{p,0}/C_s$ and Λ . Figure 10(a) shows the dependence of Sh_0 on $C_{p,0}/C_s$ for typical values of Λ from 0.1 to 10. On the whole, Sh_0 increases with the increase in $C_{p,0}/C_s$ for all Λ . Yet when $C_{p,0}/C_s < 10$, the increase in Sh_0 is not obvious. Apparent increase is only observed when $C_{p,0}/C_s > 10$. The magnitude of increase is still smaller than that caused by Λ . In applications that has lower requirement for accuracy, Sh_0 can be considered independent of $C_{p,0}/C_s$. Figure 10(b) shows the variation of Sh_0 with Λ for $C_{p,0}/C_s$ from 0.01 to 100. Since Sh_0 is less dependent on $C_{p,0}/C_s$, all the curves are highly similar in shape and close to each other. The curves exhibit an asymmetric parabola-like shape with a minimum at $\Lambda = 1$, suggesting that Sh_0 is larger for smaller Λ when $\Lambda < 1$, and Sh_0 is larger for larger Λ when $\Lambda > 1$. The simple and highly similar curve shapes facilitate the development of simple empirical models for practical applications.

For spherical particles, the surface flux $N_S^{"}$ is also calculated with diffusion layer thickness (δ) as,

$$N_S'' = D_m \frac{(C_S - C_b)}{\delta(t)} \tag{73}$$

where $\delta(t)$ is the thickness of a virtual layer surround the particle with higher concentration, and changes with time [7,10,11]. Rearranging Eqn. (73), $\delta(t)$ is written as,

$$\delta(t) \equiv D_m \frac{(C_s - C_b)}{N_s^{"}} \tag{74}$$

For spherical particles, $\delta(t)$ is roughly equal to particle radius. For prolate and oblate particles, N_S is not uniform on particle surface. To emphasize the enhancement of dissolution rate due to the change of particle shape, $\delta(t)$ can be defined as,

$$\delta(t) = D_m \frac{(c_s - c_b)}{\int_{A_n} N_s^{"} dA_p / 4\pi R_p^2} = \frac{R_p}{Sh}$$
 (75)

 $\delta(t)$ is then normalized with R_p as

$$\frac{\delta(t)}{R_n} = \frac{1}{Sh} \tag{76}$$

As particle shape changes from spherical to prolate spheroidal or oblate spheroidal, the increase in Sh leads to the decreases in $\delta(t)/R_p$. Thus, the dissolution rate is enhanced. The analysis of Sh can be easily extended to $\delta(t)/R_p$.

(e) Prediction of dissolution time

Figure 7 and 8 suggest that the end of a dissolution process is either complete dissolution $(C_{p,0}/C_s < 1)$ or saturation $(C_{p,0}/C_s > 1)$. When $C_{p,0}/C_s > 1$, the dissolution is significantly slowed down when C_b/C_s is close to 1. A considerable amount of time is consumed yet C_b/C_s changes very little. Here the dissolution time (T) is defined as the time it takes for the particle to completely dissolve when $C_{p,0}/C_s < 1$, or the time it takes for the bulk concentration (C_b/C_s) to reach 0.99 when $C_{p,0}/C_s \ge 1$. Figure 11 shows the normalized dissolution time (T/τ_{diss}) versus $C_{p,0}/C_s$ for various aspect ratio (Λ) from 1/10 to 10. As shown in the figure, all the curves exhibit similar shapes over the entire range of $C_{p,0}/C_s$ from 10^{-2} to 10^2 in the log-log scales. For each $C_{p,0}/C_s$, T/τ_{diss} of the spherical particle is the largest. According to the curve variation, four regimes of $C_{p,0}/C_s$ can be identified. In regime I $(C_{p,0}/C_s < 10^{-1})$, the initial particle concentration (C_b/C_s) is small, which makes the bulk concentration (C_b/C_s) also low throughout the dissolution process. The dissolution is close to that of a particle in an infinitely-large media. For spherical particle $(\Lambda = 1)$, it is $T/\tau_{diss} = 1$. In this regime $\log(T/\tau_{diss})$ is roughly constant

for each Λ . In regime II $(10^{-1} < C_{p,0}/C_s \le 1)$, the effect of C_b appears, which reduces the dissolution rate and increases the dissolution time. As a result, $\log(T/\tau_{diss})$ increases with the increase in $\log(C_{p,0}/C_s)$, and reaches the maximum at $C_{p,0}/C_s = 1$. When $C_{p,0}/C_s > 1$, the solution is saturated in the end. For larger $C_{p,0}/C_s$, the larger particle surface area saturates the solution faster, so $\log(T/\tau_{diss})$ decreases with the increase in $C_{p,0}/C_s$. In regime III $(1 \le C_{p,0}/C_s \le 2)$, $C_{p,0}/C_s$ is close to 1 and some nonlinear features are exhibited, so the curves are not straight. In regime IV $(C_{p,0}/C_s > 2)$, $\log(T/\tau_{diss})$ changes linearly with $\log(C_{p,0}/C_s)$ and all curves are straight lines. The curve slope is determined by the material properties, that is, $v_m C_s$.

Figure 12 shows the variation of dissolution time (T/τ_{diss}) with particle aspect ratio (Λ) for typical values of $C_{p,0}/C_s$. All the curves exhibit similar shapes in log-log scales. For each $C_{p,0}/C_s$, the maximum of T/τ_{diss} is reached at $\Lambda=1$. For prolate particles T/τ_{diss} decreases as Λ decreases, and for oblate particles T/τ_{diss} decreases as Λ increases. This is consistent with the Sherwood number shown in Fig. 10. When we plot $\log(T/\tau_{diss}) - \log(T/\tau_{diss})_{\Lambda=1}$ vs. Λ in Fig. (12b), all the curves fit together perfectly. This suggests that the effects of $C_{p,0}/C_s$ and Λ on the dissolution time can be decoupled,

$$T/\tau_{diss} = f(C_{p,0}/C_s)g(\Lambda)$$
(77)

where f and g are two functions to be determined.

(f) Effects of material properties

The nondimensional set of equations (Eqns. (13-20)) show that the dissolution process is also determined by the material properties, $C_{sat}v_m$. The above analysis was carried out with felodipine, the value of $C_{sat}v_m$ is 2.36×10^{-7} . To explore the effect of $C_{sat}v_m$ on the dissolution, some virtual particle materials with $\Pi \equiv C_{sat}v_m/(C_{sat}v_m)_{felo} = 0.01, 0.1, 10$, and 100 are compared with felodipine, where the subscript 'felo' indicates the quantities of felodipine.

Figure 13 shows the variation of initial Sherwood number (Sh_0) with initial particle concentration $(C_{p,0}/C_s)$ and particle aspect ratio (Λ) for different $C_{sat}v_m/(C_{sat}v_m)_{felo}$. As shown in Fig. 13(a), for each $C_{p,0}/C_s$ and Λ , $(Sh_0)_{\Pi=100} > (Sh_0)_{\Pi=10} > (Sh_0)_{\Pi=10} > (Sh_0)_{\Pi=0.1} > (Sh_0)_$

 $(Sh_0)_{\Pi=0.01}$. The deviation of Sh_0 from that of felodipine increases with the increase in $C_{p,0}/C_s$. When $C_{p,0}/C_s < 1$, the deviation is not apparent. Figure 13(b) shows the dependence of Sh_0 on Λ . The deviation of Sh_0 only appears for larger $C_{p,0}/C_s$ and larger Π . This is consistent with Fig. 13(a).

We also study the effect of Π on dissolution time (T/τ_{diss}) . Figure 14 shows the comparison of T/τ_{diss} versus $C_{p,0}/C_s$ for different Π . Over the most range of $C_{p,0}/C_s$, the curves are almost on top of each other for $\Lambda=1$, 1/10, and 10. The deviation appears apparently only when $C_{p,0}/C_s>10$. This is confirmed by the variation of (T/τ_{diss}) with Λ shown in Fig. 15. It should be noted that the magnitude of deviation is small because the plots are prepared in log-log scales.

4. Conclusion

In this paper, we have extended the quasi steady-state model of the dissolution of a single spherical particle to that of a prolate and an oblate spheroidal particle, based on the exact solution of the steady-state diffusion equation for mass transfer in an unconfined media. With an appropriate treatment of bulk concentration, this model can predict the detailed dissolution process of a single spheroidal particle in a container of finite size.

The dimensionless governing equations suggest that the dissolution process is determined by three dimensionless control parameters, initial solid particle concentration, particle aspect ratio, and the product of specific volume of solid particles and saturation concentration of the dissolved substance. Using this model, we have analyzed the dissolution process of felodipine particles in a broad range of space of the three control parameters and identified some characteristics. It has been found that both prolate and oblate spheroidal particles have a larger dissolution rate than spherical particles. The Sherwood number, characterized as the nondimensional dissolution rate, has been found to have a strong dependence on particle aspect ratio. For prolate spheroidal particles with smaller aspect ratio, the Sherwood number is larger, yet for oblate spheroidal particle with larger aspect ratio, the Sherwood number is larger. The Sherwood number is little influenced by the initial particle concentration. We have also examined the dissolution time. A similarity of the variation of dissolution time with particle aspect ratios for different initial particle concentrations

has been found in the logarithm scales. In the end, the effects of material properties, that is, the product of specific volume of solid particles and saturation concentration are analyzed. It has been found that the effects of material properties only appear when the initial particle concentration is much larger than the saturation concentration and the product of the particle is much larger than that of felodipine. All these characteristics facilitate the development of easy and reliable empirical models for practical applications.

The model and the analysis are also applicable to the system of monodisperse spheroidal particles of the same shape.

Data accessibility. The data that support the findings of this study are available from the corresponding author upon reasonable request.

Competing interests. We declare we have no competing interests.

Funding. This work was supported by the National Science Foundation (Award ID: 2138740)

References

- N. Salehi, J. Al-Gousous, D.M. Mudie, G.L. Amidon, R.M. Ziff, and G.E. Amidon, Hierarchical mass transfer analysis of drug particle dissolution, highlighting the hydrodynamics, pH, particle size, and buffer effects for the dissolution of ionizable and nonionizable drugs in a compendial dissolution vessel, Mol. Pharm. 17, 3870 (2020).
- 2. J. Petersen, Heap leaching as a key technology for recovery of values from low-grade ores a brief review, Hydrometallurgy, **165**, 206 (2016).
- 3. K. C. Badgujar, and B. M. Bhanage, Factors governing dissolution process of lignocellulosic biomass in ionic liquid: Current status, overview and challenges, Bioresour. Technol. **178**, 2 (2015).
- 4. A. Chamolly and E. Lauga, Stochastic dynamics of dissolving active particles, Eur. Phys. J. E. 42,1 (2019).

- 5. D. Hörter and J. B. Dressman, Influence of physicochemical properties on dissolution of drugs in the gastrointestinal tract, Adv. Drug Deliv. Rev, **46**, 75 (2001).
- 6. S. S. Jambhekar and P. J. Breen, Drug dissolution: significance of physicochemical properties and physiological conditions, Drug Discov. Today, **18**, 1173 (2013).
- 7. P. Costa and J. M. S. Lobo, Modeling and comparison of dissolution profiles, Eur. J. Pharm. Sci. **13**, 123 (2001).
- 8. V. Mandar and J. T. Carstensen, Effect of change in shape factor of a single crystal on its dissolution behavior, Pharm. Res. **13**,155 (1996).
- 9. A. T. K. Lu, M. E. Frisella, and K. C. Johnson, Dissolution modeling: factors affecting the dissolution rates of polydisperse powders, Pharm. Res. **10**,1308 (1993).
- 10. R. J. Hintz and K. C. Johnson, The effect of particle size distribution on dissolution rate and oral absorption, Int. J. Pharm. **51**, 9 (1989).
- 11. J. J. Sheng, P. J. Sirois, J. B. Dressman, and G. L. Amidon, Particle diffusion layer thickness in a USP dissolution apparatus II: A combined function of particle size and paddle speed, J. Pharm. Sci. 97, 4815 (2008).
- 12. W. Zhong, A. Yu, G. Zhou, J. Xie and H. Zhang, CFD simulation of dense particulate reaction system: Approaches, recent advances and applications, Chem. Eng. Sci. **140**, 16 (2016).
- 13. W. Zhong, A. Yu, X. Liu, Z. Tong and H. Zhang, DEM/CFD-DEM modelling of non-spherical particulate systems: theoretical developments and applications. Pow. Tech. **302**, 108 (2016).
- 14. N. Salehi, J. Al-Gousous, D.M. Mudie, G.L. Amidon, R.M. Ziff, Hierarchical mass transfer analysis of drug particle dissolution, highlighting the hydrodynamics, pH, particle size, and buffer effects for the dissolution of ionizable and nonionizable drugs in a compendial dissolution vessel, Mole. Pharm. 17, 3870 (2020).
- 15. Y. Wang, B. Abrahamsson, L. Lindfors and J. G. Brasseur, Comparison and analysis of theoretical models for diffusion-controlled dissolution, Mole. Pharm. 9, 1052 (2012).
- 16. L. Lindfors, M. Jonsson, E. Weibull, J. G. Brasseur and B. Abrahamsson, Hydrodynamic effects on drug dissolution and deaggregation in the small intestine-A study with felodipine as a model drug, J. Pharm. Sci. 104, 2969 (2015).

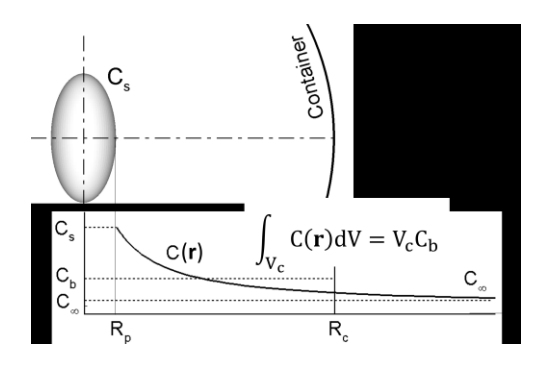


Figure 1. Illustration of quasi steady-state model for a single particle in a container of finite size.

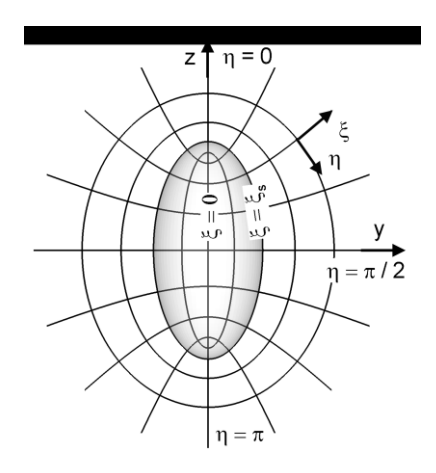


Figure 2. The prolate spheroidal coordinates.

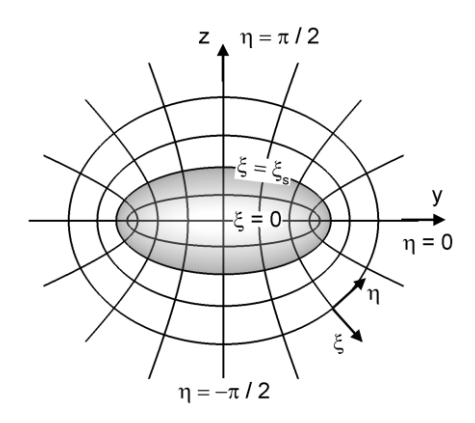


Figure 3. The oblate spheroidal coordinates.

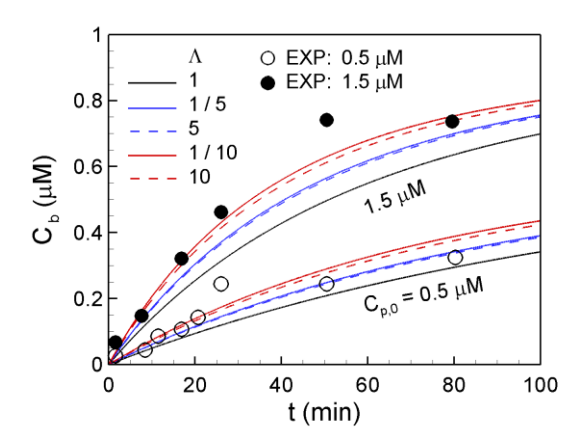


Figure 4. Comparison between QSM predictions and in vitro experiments.

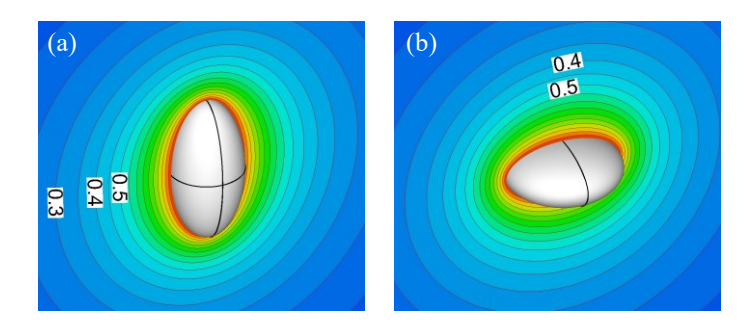


Figure 5. Normalized concentration $((C - C_{\infty})/(C_s - C_{\infty}))$ around a spheroidal particle. (a) prolate $(\Lambda = 0.5)$, and (b) oblate $(\Lambda = 2)$.

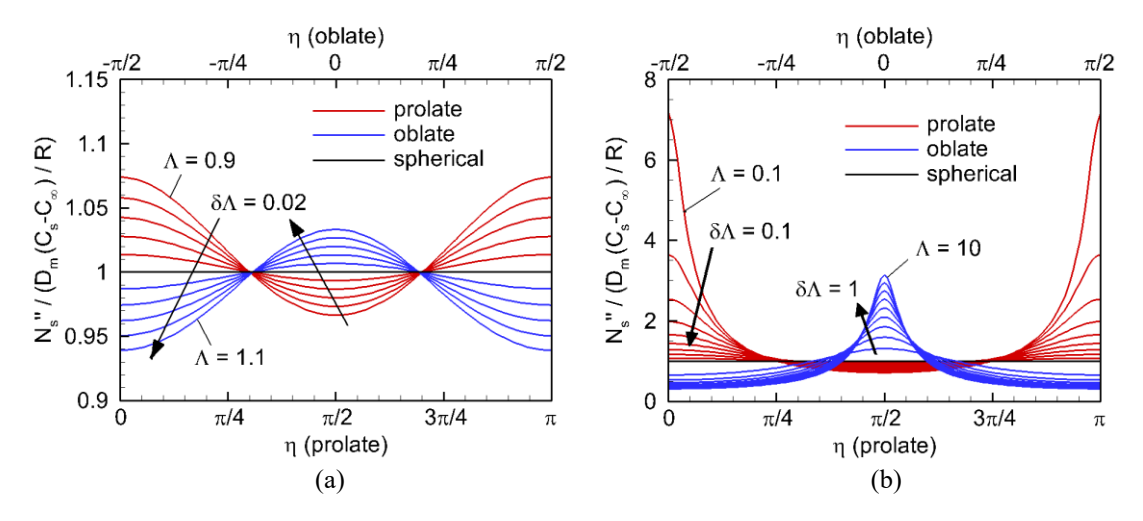


Figure 6. Variation of release flux at particle surfaces for various aspect ratios (Λ), (a) from 0.9 to 1.1, and (b) from 0.1 to 10.

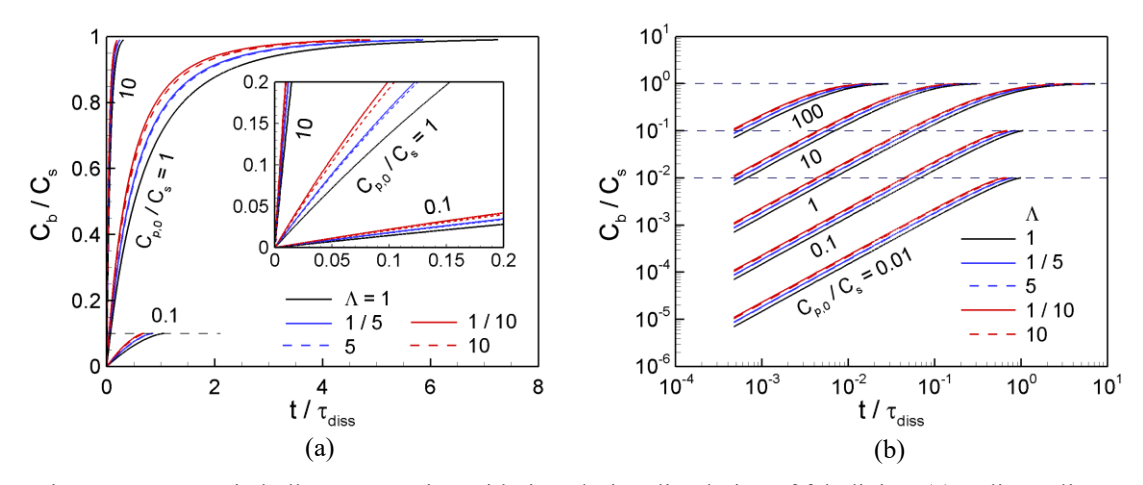


Figure 7. Increase in bulk concentration with time during dissolution of felodipine. (a) In linear-linear scales, and (b) in log-log scales

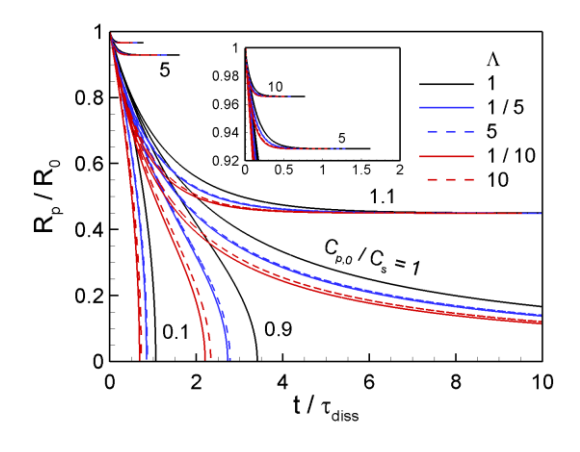


Figure 8. Decrease in equivalent particle radius with time during dissolution of felodipine.

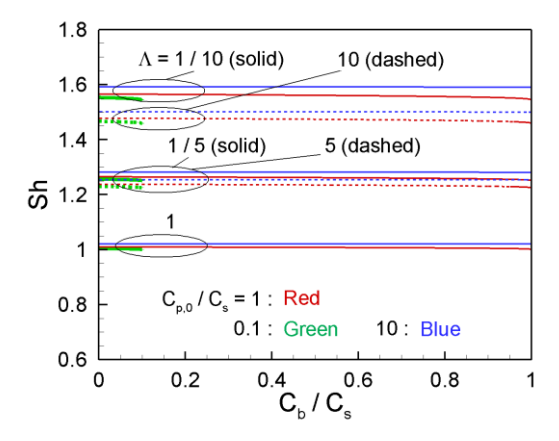


Figure 9. Variation of Sherwood number with bulk concentration during dissolution of felodipine.

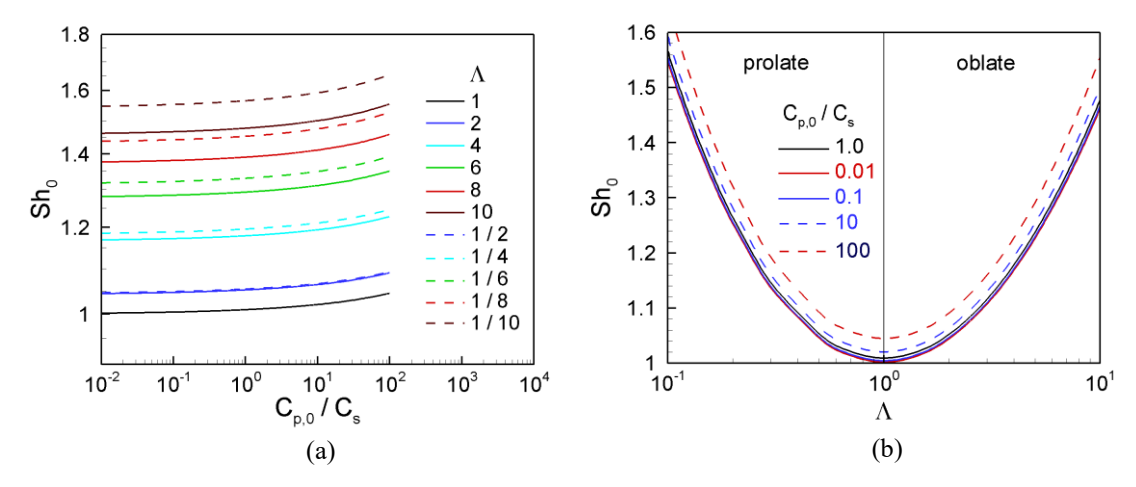


Figure 10. Initial Sherwood number versus (a) initial concentration of solid particles and (b) particle aspect ratio.

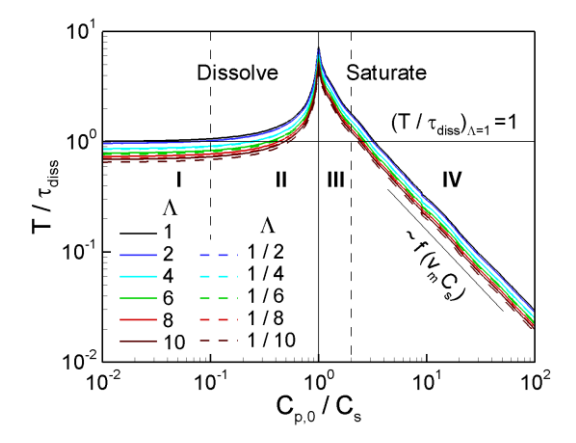


Figure 11. Variation of dissolution time with initial concentration of solid particles.

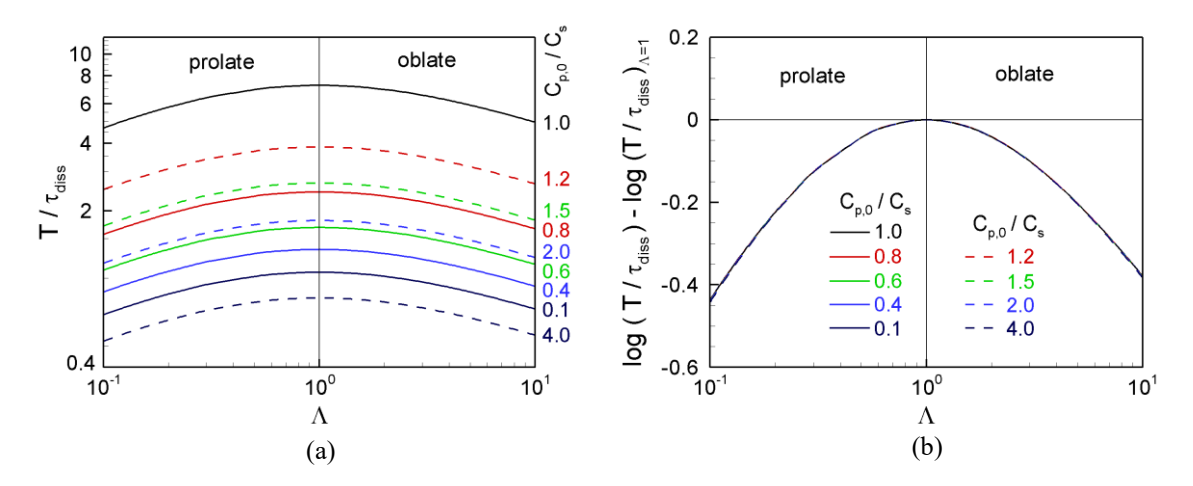


Figure 12. Variation of dissolution time with particle aspect ratio. (a) T/τ_{diss} vs. Λ , and (b) $\log(T/\tau_{diss}) - \log(T/\tau_{diss})_{\Lambda=1}$ vs. Λ

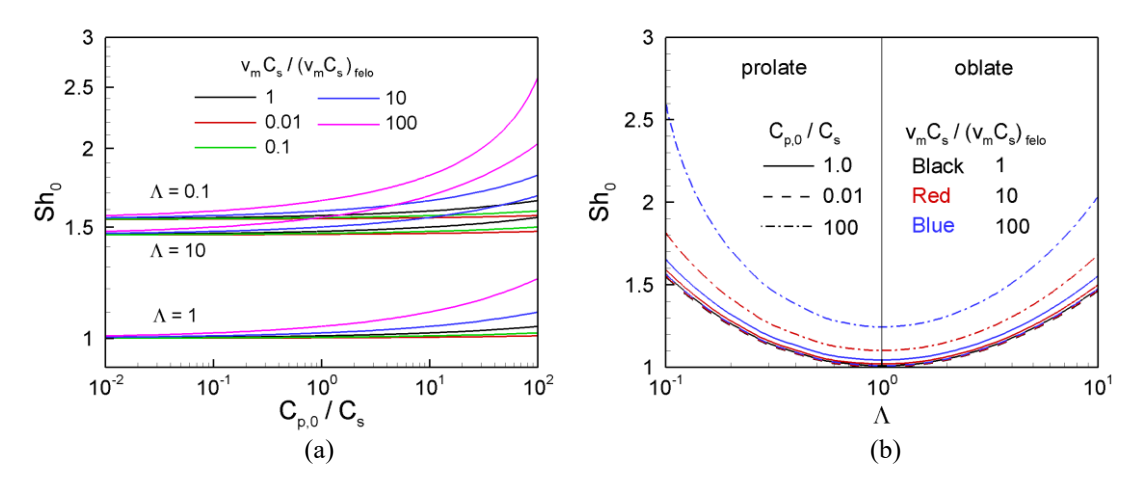


Figure 13. Effects of $v_m C_s$ on initial Sherwood number against (a) initial concentration of solid particles and (b) particle aspect ratio.

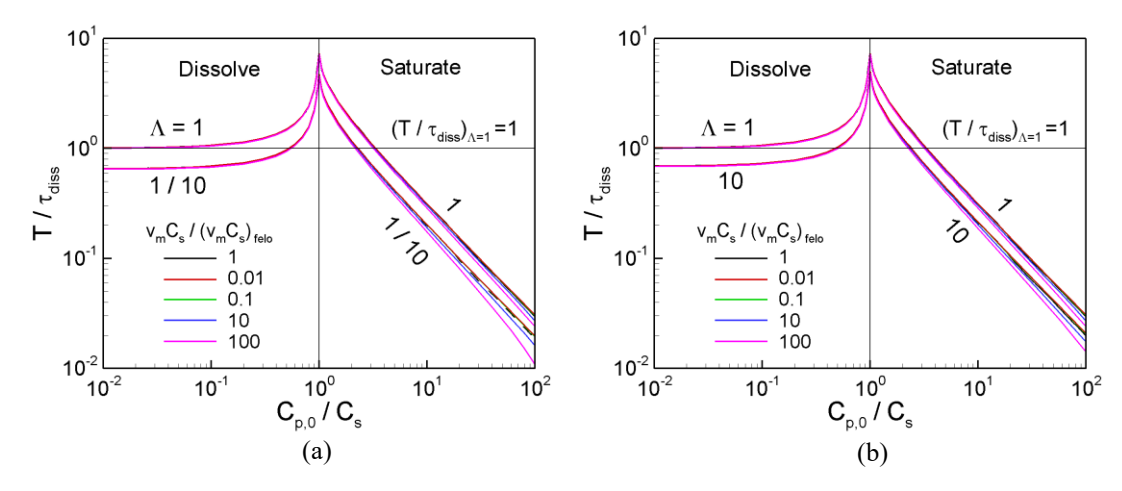


Figure 14. Effects of $v_m C_s$ on dissolution time against initial concentration of solid particles.

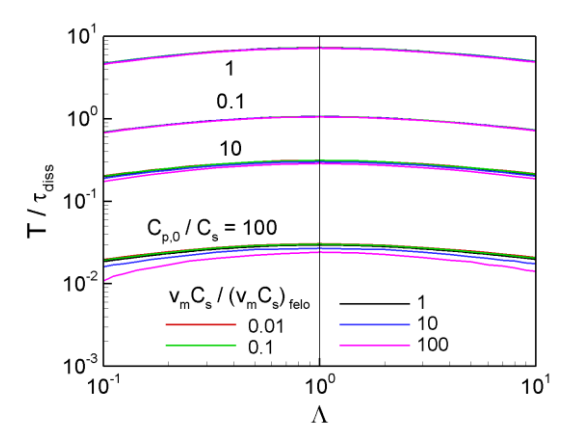


Figure 15. Effects of $v_m C_s$ on dissolution time against particle aspect ratio.